# Fault Rupture Propagation through Sand: Finite-Element Analysis and Validation through Centrifuge Experiments

I. Anastasopoulos[1]; G. Gazetas, M.ASCE[2]; M. F. Bransby[3]; M. C. R. Davies[4]; and A. El Nahas[5]

**Abstract:** The three notorious earthquakes of 1999 in Turkey (Kocaeli and Düzce) and Taiwan (Chi-Chi), having offered numerous examples of surface fault rupturing underneath civil engineering structures, prompted increased interest in the subject. This paper develops a nonlinear finite-element methodology to study dip–slip ("normal" and "reverse") fault rupture propagation through sand. The procedure is verified through successful Class A predictions of four centrifuge model tests. The validated methodology is then utilized in a parametric study of fault rupture propagation through sand. Emphasis is given to results of engineering significance, such as: (1) the location of fault outcropping; (2) the vertical displacement profile of the ground surface; and (3) the minimum fault offset at bedrock necessary for the rupture to reach the ground surface. The analysis shows that dip–slip faults refract at the soil–rock interface, initially increasing in dip. Normal faults may keep increasing their dip as they approach the ground surface, as a function of the peak friction angle $\varphi_p$ and the angle of dilation $\psi_p$. In contrast, reverse faults tend to decrease in dip, as they emerge on the ground surface. For small values of the base fault offset, $h$, relative to the soil thickness, $H$, a dip–slip rupture cannot propagate all the way to the surface. The $h/H$ ratio required for outcropping is an increasing function of soil "ductility." Reverse faults require significantly higher $h/H$ to outcrop, compared to normal faults. When the rupture outcrops, the height of the fault scrap, $s$, also depends on soil ductility.

## Introduction

In a seismic event, the rupture of an earthquake fault generates two types of ground displacement: permanent quasistatic offsets on the fault itself, and transient dynamic oscillations away from the fault (Ambraseys and Jackson 1984). The second type of displacement is the result of waves originating successively at each "point" on the fault (as "slippage" takes place) and propagates over large distances in the earth. Such waves always affect the ground surface and are thus of prime significance for the safety of civil engineering structures. By contrast, the permanent offset on a fault affects the ground surface only in some cases—when the fault rupture extends all (or nearly all) the way to the surface.

Naturally, therefore, earthquake engineering research and practice has (over the last four decades) emphasized the dynamic response of soil and structural systems to ground oscillations. Much less effort has been devoted to understanding the effect of a rock-rupturing seismic fault on the overlying soil and on the structures and facilities founded on or in it. The three notorious 1999 earthquakes in Turkey and Taiwan (Kocaeli, Düzce, and Chi-Chi), having offered numerous examples of detrimental effects of (large) surface fault ruptures, prompted the increased interest on the subject.

The main goal of this paper is to present an in-depth numerical analysis of the whole phenomenon of fault rupture propagation from the base rock to the ground surface. Verification of the developed numerical methodology against centrifuge experiments gives the necessary confidence for the validity of our numerical results. More specifically, the present paper:

1. Develops a finite-element modeling technique to analyze dip–slip (normal and reverse) fault rupture propagation through sand;
2. Validates the developed analysis methodology through successful Class A predictions of four centrifuge experiments conducted at the University of Dundee; and
3. Studies parametrically the propagation of dip–slip fault ruptures through sand, emphasizing the deformation of the ground surface.

## Finite-Element Modeling Methodology

Attempts to utilize the finite-element (FE) method to model the propagation of a fault rupture through soil have been recently reported in the literature. One of the first such studies, by Bray et al. (1994a), concluded that FE modeling can be successful if certain conditions are satisfied, such as the use of a refined mesh

[1]Postdoctoral Researcher, National Technical Univ., Athens, Zografou 15342, Greece.

[2]Professor, National Technical Univ., Athens, Zografou 15342, Greece.

[3]Senior Lecturer, Univ. of Dundee, Nethergate, Dundee DD1 4HN, Scotland, U.K.

[4]Professor, Univ. of Dundee, Nethergate, Dundee DD1 4HN, Scotland, U.K.

[5]Formerly, Postdoctoral Researcher, Univ. of Dundee, Nethergate, Dundee DD1 4HN, Scotland, U.K.
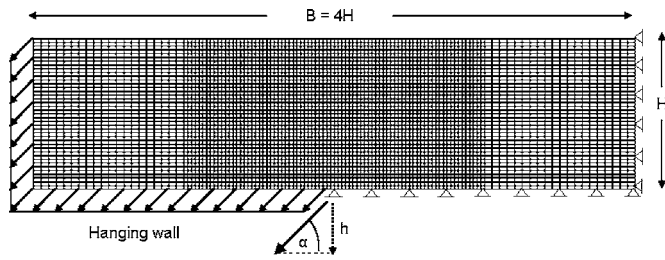
**Fig. 1.** Problem geometry, finite-element discretization, and imposed normal faulting boundary conditions



**Fig. 2.** Variation of mobilized friction angle $\varphi_{mob}$ and dilation $\psi_{mob}$ with octahedral plastic shear strain
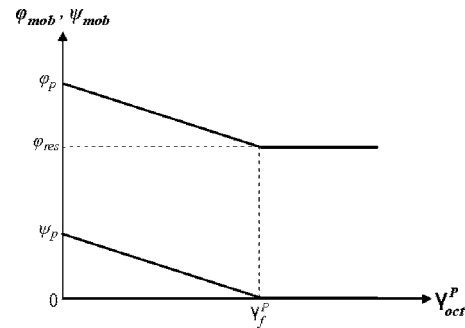
in the neighborhood of the potential rupture and the use of a nonlinear constitutive law for the soil.

The problem studied here and the FE discretization are displayed in Fig. 1. It refers to a uniform soil deposit of thickness $H$ at the base of which a dip–slip fault, dipping at an angle $a$ (measured from the horizontal), ruptures and produces downward or upward displacement, with a vertical component $h$. Following the recommendation of Bray (1990), the width of the FE model was set to $B=4H$ to minimize undesired parasitic boundary effects. The appropriateness of this selection was verified through an accompanying sensitivity study (Anastasopoulos 2005). As shown in Fig. 1, the discretization is finer in the central part of the model, with the quadrilateral elements being 1 m×1 m (width ×height). This selection was also made following the outcome of the aforementioned sensitivity study. Near the two sides of the model, where the deformation is expected to be limited, the mesh is coarser: 2 m×1 m. The differential displacement (hereafter called "offset," or "dislocation") is applied to the left part of the model quasistatically in small consecutive steps.

## Constitutive Model

Several experimental and numerical studies have shown that post-peak soil behavior is a decisive factor in fault rupture propagation and its possible emergence on the ground surface (Cole and Lade 1984; Lade et al. 1984). Scott and Schoustra (1974) utilizing the FE method and an elastic–perfectly plastic constitutive soil model with Mohr–Coulomb failure criterion, produced results contradicting both reality and experiments. Walters and Thomas (1982) employed a more elaborate nonlinear incremental constitutive model with Drucker–Prager failure criterion, nonassociated flow rule, and strain softening to simulate reverse fault rupture propagation through cohesionless soil. Comparing their analysis results with benchmark small-scale tests, they proved that (laboratory) reality could only be reproduced with a nonassociated flow rule and strain softening. Bray (1990) and Bray et al. (1994a,b), utilizing a FE code with a hyperbolic nonlinear elastic constitutive law, also achieved satisfactory agreement with experiments (Bray et al. 1993). Also successful were the analyses performed by Roth et al. (1982), White et al. (1994), Nakai et al. (1995), Loukidis (1999), and Erickson et al. (2001), all of which made use of the finite-difference (FD) method with an elastoplastic constitutive model, Mohr–Coulomb failure criterion, and strain softening.

Similar constitutive models have been employed successfully to model the failure of embankment dams and the delayed collapse of cut slopes in stiff clay (Potts et al. 1990, 1997). Following a thorough review of the literature (Anastasopoulos 2005), we adopted a similar elastoplastic Mohr–Coulomb constitutive model with isotropic strain softening. As depicted in Fig. 2, strain soft-

ening is introduced by reducing the mobilized friction angle $\varphi_{mob}$ and the mobilized dilation angle $\psi_{mob}$ with the increase of octahedral plastic shear strain

$$\varphi_{mob} = \begin{cases} \varphi_p - \dfrac{\varphi_p - \varphi_{res}}{\gamma_f^P}\gamma_{oct}^P & \text{for } 0 \leq \gamma_{oct}^P < \gamma_f^P \\ \varphi_{res} & \text{for } \gamma_{oct}^P \geq \gamma_f^P \end{cases} \quad (1)$$

$$\psi_{mob} = \begin{cases} \psi_p\left(1 - \dfrac{\gamma_{oct}^P}{\gamma_f^P}\right) & \text{for } 0 \leq \gamma_{oct}^P < \gamma_f^P \\ \psi_{res} & \text{for } \gamma_{oct}^P \geq \gamma_f^P \end{cases} \quad (2)$$

where $\varphi_p$ and $\varphi_{res}$=ultimate mobilized friction angle and its residual (or critical state) value; $\psi_p$=ultimate dilation angle; and $\gamma_f^P$=plastic octahedral shear strain at which softening has been completed.

The model is incorporated in the finite-element code ABAQUS (2004) through a user subroutine. Model parameters are calibrated through the direct shear test—a test closely mimicking the shearing from a fault. Although it has been severely criticized in the past for the nonuniformity of stresses and strains developing in the soil sample (Terzaghi and Peck 1948; Morgenstern and Tchalenko 1967; Saada and Townsend 1981; Budhu 1984), due to its simplicity it remains quite popular in practice. Despite the aforementioned unavoidable nonuniformities, the effect of progressive failure has been shown to be only slight (Potts et al. 1987), allowing the interpretation of test results as quasisimple shear.

Fig. 3 shows a typical variation of the stress ratio, $\tau/\sigma_v$, and volume change (expressed through vertical displacement $\delta y$ of the top platen) with respect to the imposed horizontal displacement $\delta x$ in a direct shear test of dense Toyoura sand [based on data of Shibuya et al. (1997)]. Soil response can be divided in four characteristic phases:

1. *Quasielastic behavior* (OA): Up to Point A the soil deforms quasielastically (Jewell and Roth 1987). Some nonlinearity is clearly observed, but without any dilation. $\delta x_y$ is defined as the horizontal displacement for which $-\delta y/\delta x > 0$.
2. *Plastic behavior* (AB): From Point A to B the soil "yields", enters the plastic region, and dilates. Peak conditions are reached at Point B. $\delta x_p$=horizontal displacement for which $\tau/\sigma_v$=max.
3. *Softening behavior* (BC): From Point B to C the soil experiences softening. Right after the peak, a single horizontal shear band develops at midheight of the specimen (Jewell and Roth 1987; Gerolymos et al. 2007). Softening is com-
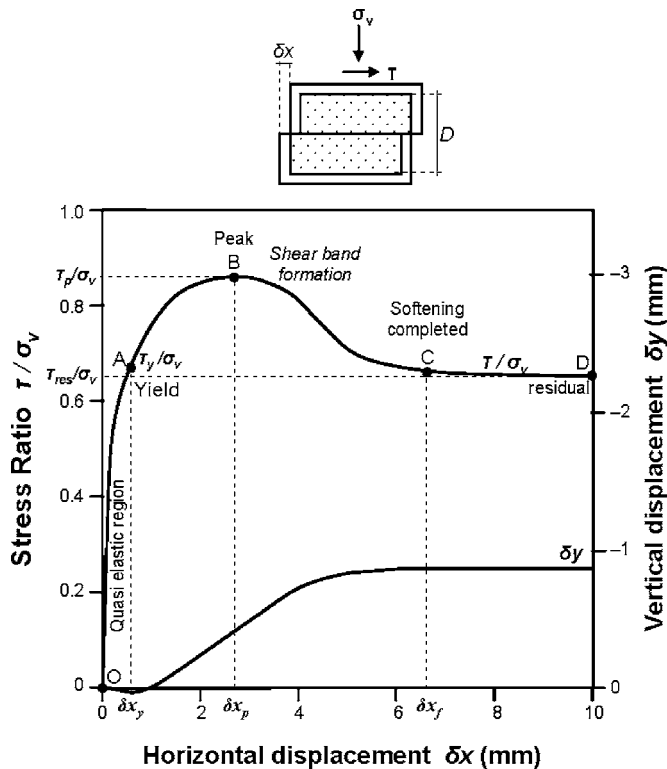
**Fig. 3.** Typical variation of stress ratio and volume change with respect to horizontal displacement in a direct shear test [dense Toyoura sand (Shibuya et al. 1997)]

pleted at Point C, and $\delta x_f$=horizontal displacement for which $-\delta y / \delta x \approx 0$.

4. *Residual behavior* (CD): Shearing is accumulated along the developed shear band.

As previously mentioned, test results can be interpreted assuming quasisimple shear. Shibuya et al. (1997) have shown that the simple shear mode needs only be developed along the shear band. The relationship between the direct shear (DS) peak $\varphi_p^{DS}$ and residual (or critical state) $\varphi_{res}^{DS}$ angle of friction can be approximated as

$$\tan(\varphi_p^{DS}) = \tan(\varphi_{res}^{DS}) + \alpha \tan(\psi_p) \qquad (3)$$

where $\alpha$=constant. With an optimum shear box apparatus (no rotation of the loading platen, smooth end walls, opening size between top and bottom platen equal to the thickness of the shear band) $\alpha$ can be taken equal to 1 (Shibuya et al. 1997). The plane strain peak angle of friction $\varphi_p$ can then be computed as (Jewell 1989)

$$\sin(\varphi_p) = \frac{\tan(\varphi_p^{DS})}{\cos(\psi_p) + \sin(\psi_p)\tan(\varphi_p^{DS})} \qquad (4)$$

Preyield behavior is modeled as linear elastic, with a secant modulus $G_S$ linearly increasing with depth

$$G_S = \frac{\tau_y}{\gamma_y} \qquad (5)$$

where $\gamma_y$ and $\tau_y$=yield shear strain and stress, respectively. While $\tau_y$ can be directly measured from the test data (the shear stress that corresponds to $\delta x_y$), to compute $\gamma_y$ a shear zone thickness needs to be assumed. Before formation of the shear band, shear strain can be assumed to be more or less uniformly distributed

throughout the whole depth, $D$, of the soil specimen. Hence, $\gamma_y$ can be defined as

$$\gamma_y = \frac{\delta x_y}{D} \qquad (6)$$

The same can be applied for the peak shear strain $\gamma_p$ (assuming that the shear band has not yet formed)

$$\gamma_p = \frac{\delta x_p}{D} \qquad (7)$$

Consequently, the plastic shear strain at peak will be

$$\gamma_p^P = \frac{\delta x_p - \delta x_y}{D} \qquad (8)$$

After formation of the shear band (i.e., right after the peak, beyond Point B), adopting the two-block model of shearing of Shibuya et al. (1997), it is assumed that all plastic shear deformation takes place within the shear band, while the rest of the soil body remains elastic. Assuming the width of the shear band, $d_B$, equal to $16d_{50}$ (Vardoulakis and Graf 1985), where $d_{50}$=mean particle size of the sand, the plastic shear strain at which softening is completed, $\gamma_f^P$, will be

$$\gamma_f^P = \gamma_p^P + \frac{\delta x_f - \delta x_p}{16d_{50}} = \frac{\delta x_p - \delta x_y}{D} + \frac{\delta x_f - \delta x_p}{16d_{50}} \qquad (9)$$

## Mesh Dependency and Scale Effects

The use of the finite-element method in combination with strain softening constitutive models may lead to mesh-dependent solutions (e.g., Pietruszezak and Mroz 1981). Such difficulties may be overcome through use of higher-order constitutive models, such as the viscoplastic model (e.g., Loret and Prevost 1990), nonlocal theory approaches (e.g., Bažant and Tsang 1984), and gradient elastoplasticity models (e.g., Mühlhaus and Vardoulakis 1987; de Borst 1991). Such models have been successfully employed to model the evolution of shear bands and the associated scale effects in laboratory experiments (Gudehus and Nübel 2004). However, to obtain mesh-independent solutions, the size of the elements has to be of the order of $3d_{50}$ (Gudehus and Nübel 2004). This means that, even for a relatively coarse sand with $d_{50}$=1 mm, the finite-elements have to be 3 mm wide. Obviously, such mesh size prohibits the application of such rigorous approaches in modeling real-scale problems. To do so, remeshing and special interface elements for the localization zones would be necessary (Gudehus and Nübel 2004). With today's computing power, such an approach would not be practical. Even if it could be achieved, the computing cost would prohibit the performance of parameter studies.

Scale effects have also proven to be substantial in shear localization problems (Stone and Muir Wood 1992; Muir Wood and Stone 1994; Muir Wood 2002) and have to be carefully addressed. Given the unavoidable shortcomings of the finite-element method, an approximate simplified scaling method is employed in this paper.

First of all, it must be clearly pointed out that shear localization can take place along one element, i.e., the width of the FE shear "band" will be equal to the size of the element, $d_{FE}$, for four-noded elements (or to half of it, for eight-noded elements). So, ideally, $d_{FE}$ should be equal to the width of the real shear band $d_B$ ($\approx 16d_{50}$). Unfortunately, due to computing time constraints
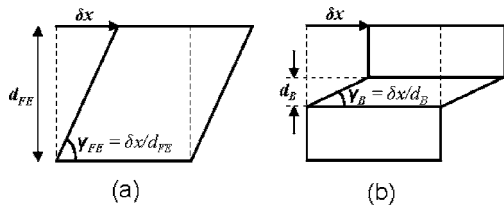
**Fig. 4.** Idealized simple shear conditions: (a) finite-element computed shear strain; (b) shear strain along the shear band (after peak conditions)

this is generally only practical when modeling laboratory-scale experiments, or if the failure surface is predefined (e.g., Potts et al. 1990). In general, $d_{FE}$, and thus the FE-predicted shear "band," will be significantly larger than the real one, $d_B$. As schematically illustrated in Fig. 4(a), assuming simple shear conditions, for a given shear displacement $\delta x$ the shear strain computed in one finite-element, $\gamma_{FE}$, will be

$$\gamma_{FE} \approx \frac{\delta x}{d_{FE}} \qquad (10)$$

At pre-shear-band conditions Eq. (10) is a reasonable simplification. In stark contrast, after formation of the shear band, the real shear strain, $\gamma_B$, will be significantly larger [Fig. 4(b)]

$$\gamma_B \approx \frac{\delta x}{d_B} \qquad (11)$$

A ratio $\lambda$ between the real and the FE-computed shear strain can be defined

$$\lambda = \frac{\gamma_B}{\gamma_{FE}} \approx \frac{\delta x/d_B}{\delta x/d_{FE}} = \frac{d_{FE}}{d_B} \qquad (12)$$

Hence, dividing $\gamma_f^P$ with the ratio $\lambda$, $\gamma_{FE}$ can be made compatible with the actual strain

$$\gamma_f^P = \gamma_p^P + \frac{\delta x_f - \delta x_p}{16 d_{50}} \frac{16 d_{50}}{d_{FE}} = \frac{\delta x_p - \delta x_y}{D} + \frac{\delta x_f - \delta x_p}{d_{FE}} \qquad (13)$$

This way, scale effects (associated with incorrect modeling of the shear band thickness) can be incorporated into the FE model in a reasonably approximate manner. Scaling is not applied to the pre-shear-band parameters $\gamma_y$ and $\gamma_p$.

## Constitutive Model Verification

To verify the capability of the modified Mohr–Coulomb constitutive model to reproduce actual soil behavior, a series of FE simulations of the direct shear test have been compared to published laboratory data. Fig. 5 illustrates an example of model calibration for medium dense $(D_r \approx 80\%)$ Fontainebleau sand $(d_{50} = 0.3$ mm$)$ based on direct shear test data by Gaudin (2002). The initial depth of the soil sample was $D = 20$ mm and the vertical effective stress $\sigma_v$ was varied from 33 to 188.5 kPa.

The direct shear peak friction angle $\varphi_p^{DS}$ for $\sigma_v = 188.5$ kPa is $\varphi_p^{DS} = \tan^{-1}(147/188.5) = 37.9°$. Similarly, the residual friction angle $\varphi_{res}^{DS}$ is $\varphi_{res}^{DS} = \tan^{-1}(110/188.5) = 30.2°$. The dilation angle is derived from the measured $-\delta y/\delta x$ (not shown herein): $\psi_p = 11°$. Then, the plane-strain peak angle of friction, $\varphi_p = 39.3°$, is computed from $\sin(\varphi_p) = \tan(37.9)/[\cos(11) + \sin(11)\tan(37.9)]$. Displacements $\delta x_y$, $\delta x_p$, and $\delta x_f$ are directly deduced from the
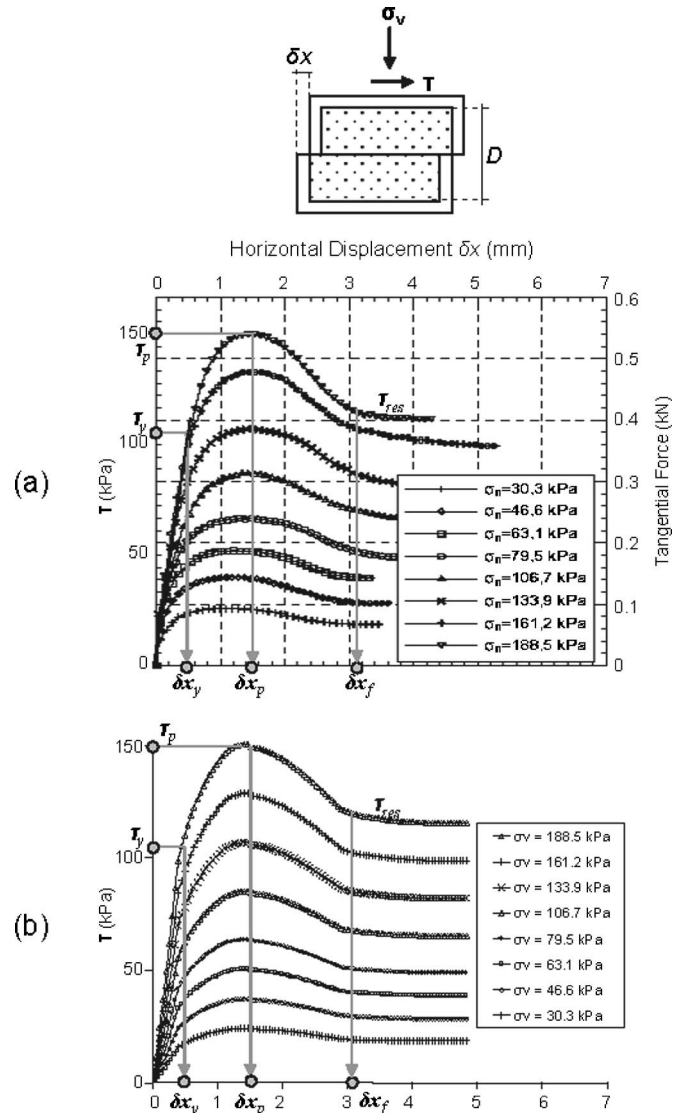


**Fig. 5.** Comparison between (a) laboratory direct shear tests on Fontainebleau sand (Gaudin 2002); (b) the results of the constitutive model utilized in the analysis

measured data: $\delta x_y \approx 0.4$ mm, $\delta x_p \approx 1.5$ mm, and $\delta x_f \approx 3.1$ mm. Then, $\gamma_y$ and $\gamma_p$ are computed from Eqs. (6) and (8), respectively: $\gamma_y = 0.4/20 = 0.02$ and $\gamma_p^P = (1.5-0.4)/20 = 0.055$. Finally, for $d_{FE} = 20$ mm selected for the analysis, Eq. (13) yields $\gamma_f^P = 0.055 + (3.1-1.5)/20 = 0.135$.

As illustrated in Fig. 5, the comparison between simulated and laboratory curves is quite satisfactory. In conclusion, despite its simplicity and (perhaps) lack of generality, the constitutive model can capture adequately the predominant mode of deformation of the specific problem studied herein—a reasonable simplification to a complex soil behavior.

## Modeling Methodology Verification: Class A Prediction of Centrifuge Model Tests

### Configuration of Centrifuge Models

A set of centrifuge model tests were conducted in the beam centrifuge at the University of Dundee. Both normal and reverse fault
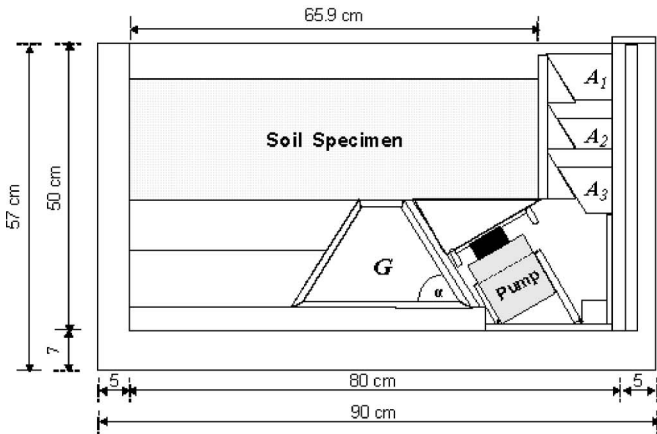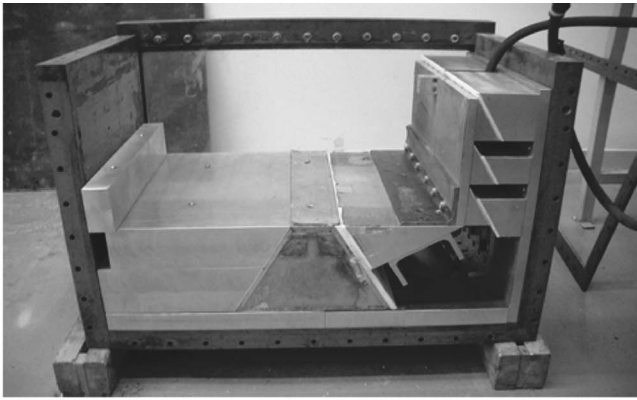
**Fig. 6.** Photograph and basic dimensions of the experimental apparatus that was installed in the Dundee University centrifuge to simulate dip–slip fault rupture propagation through soil

ruptures were modeled at centrifugal accelerations ranging from 50 to 115$g$. A study on the effect of stress level on fault rupture propagation is reported by El Nahas et al. (2006). A special experimental apparatus was developed in Dundee to simulate the faulting process (Fig. 6). The internal width of the apparatus is 65.9 cm, with external dimensions of 90 cm $\times$ 57 cm (width $\times$ height). An oil pump was utilized to transfer oil into two hydraulic cylinders acting as linear actuators. These actuators pushed the right part of the apparatus up or down, to simulate reverse and normal faulting, respectively. At the right part of the apparatus, in addition to the main central guidance system (denoted as $G$), three aluminum wedges ($A_1$, $A_2$, and $A_3$) were installed to ensure that the displacement was imposed at the desired dip angle (60° in the case presented here). At both sides of the apparatus Perspex windows were installed so that the propagation of the rupture could be observed. A digital camera captured, typically, 30 images of the deformed soil specimen as the imposed bedrock displacement increased. Image analysis was achieved using the Geo-PIV program of White et al. (2003) to compute vertical and horizontal displacements at different positions within the soil. Additional postprocessing allowed calculation of displacement profiles and strains within the deforming soil for different imposed (bedrock) displacements $h$.

Before conducting four of these experiments, Class A predictions (Lambe 1973) were conducted to validate the robustness of the modeling methodology. Fontainebleau sand (Gaudin 2002) was utilized for all experiments. The specimens were prepared by raining the sand from a specific height with controllable mass flow rate: both affect the density of the prepared sand. Two nor-

**Table 1.** Summary of Basic Parameters and Prototype Dimensions of Centrifuge Experiments

| Test | Fault type | $g$ level[a] | $D_r$ (%) | $H$ (m) | $L$ (m) | $W$ (m) | $h_{max}$ (m) |
|------|-----------|-----------|-----------|---------|---------|---------|---------------|
| 4 | Normal | 100 | 80.0 | 25.0 | 68.0 | 20.0 | 1.91 |
| 3 | Reverse | 100 | 83.9 | 25.0 | 68.0 | 20.0 | 2.22 |
| 12 | Normal | 115 | 60.2 | 24.7 | 75.7 | 23.5 | 3.15 |
| 8 | Reverse | 115 | 60.9 | 24.5 | 75.7 | 23.5 | 2.56 |

[a]Centrifugal acceleration.

mal and two reverse fault ruptures at $\alpha = 60°$ on dry medium-loose and dry medium-dense sand were selected for the computations:

- Test 4: Normal faulting on medium-dense Fontainebleau sand ($D_r \approx 80\%$);
- Test 3: Reverse faulting on medium-dense Fontainebleau sand ($D_r \approx 80\%$);
- Test 12: Normal faulting on medium-loose Fontainebleau sand ($D_r \approx 60\%$); and
- Test 8: Reverse faulting on medium-loose Fontainebleau sand ($D_r \approx 60\%$).

More details on the basic parameters and dimensions of the experiments are given in Table 1 and Fig. 7. The depth of the prototype soil deposit was kept constant, $H = 25$ m, while the other dimensions $W$, $L$ were varied, depending on the centrifugal acceleration level: $L = 68$ m for tests conducted at 100$g$; $L = 75.7$ m for tests conducted at 115$g$. The basic similarity laws between model and prototype are summarized in Table 2 [after Muir Wood (2004)]. Earlier tests (3 and 4) were conducted at 100$g$, while the later (8 and 12) at 115$g$ to allow larger maximum imposed offset, $h_{max}$, in prototype scale (with the same capacity of the oil pump). Note also that the hanging wall in the centrifuge model tests is to the right.

## Experimental Results versus Theoretical Predictions

### Tests 4 and 3: Medium-Dense Fontainebleau Sand

The two tests were conducted at 100$g$ centrifugal acceleration, with the former (Test 4) referring to normal and the latter (Test 3) to reverse faulting. For the numerical predictions we have used $\varphi_p = 39°$, $\varphi_{res} = 30°$, $\psi_p = 11°$, and $\gamma_y = 0.02$, following the previously discussed calibration procedure (Fig. 5). The calibration of $\gamma_f^P$ depends on $d_{FE}$, and is thus different from what was mentioned before for the simulation of the direct shear test. Since $d_{FE}$ is now
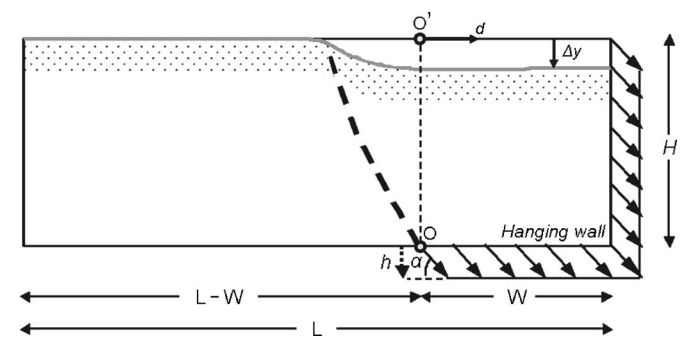


**Fig. 7.** Basic model dimensions and definitions for the centrifuge tests (normal faulting)

**Table 2.** Summary of Basic Scale Factors [after Muir Wood (2004)]

| Quantity | Laboratory (1g) | Centrifuge (ng) |
|---|---|---|
| Length | $1/n$ | $1/n$ |
| Mass density | 1 | 1 |
| Stress | $1/n$ | 1 |
| Strain | $1/n^{1-\alpha}$ | 1 |
| Displacement | $1/n^{2-\alpha}$ | $1/n$ |

equal to 1 m (=1,000 mm), Eq. (13) yields: $\gamma_f^P=0.055+(3.1-1.5)/1,000=0.0566$. This value would be reasonable to simulate reality (i.e., the prototype). However, to be in accord with the centrifuge model, it must be taken into account that the grain size is not scaled down in the centrifuge. This means that, in terms of $d_{50}$, the sand modeled in the centrifuge corresponds to a prototype material with mean particle size equal to $nd_{50}$, where $n$ = scale factor (equal to the centrifugal acceleration). Hence, for $n=100$ the model sand corresponds to a prototype material with grain size equal to $100d_{50}$ (=30 mm for the Fontainebleau sand of the conducted experiments). Thus, to model the experiment correctly, Eq. (13) must be converted

$$\gamma_f^P = \gamma_p^P + \frac{\delta x_f - \delta x_p}{16d_{50}}\frac{n16d_{50}}{d_{FE}} = \frac{\delta x_p - \delta x_y}{D} + \frac{\delta x_f - \delta x_p}{d_{FE}}n \quad (14)$$

So, for $n=100$, Eq. (14) yields $\gamma_f^P=0.055+100(3.1-1.5)/1,000=0.215$. Obviously, if the aim was to model reality, $n$ should be taken equal to 1.

Analysis predictions are compared with centrifuge experiment results in terms of the vertical displacement profile of the ground surface. Additionally, images from the experiments are compared to the FE deformed mesh with plastic strain.

A characteristic image from Test 4 (normal faulting) is compared to the deformed mesh of the analytical prediction in Fig. 8(a). Note that despite a small difference between the imposed displacements in the FE analysis and the centrifuge model test (for the analysis, $h=1$ m exactly, but the snapshot was captured at $h\approx1.08$ m), their agreement is satisfactory. The only difference between prediction and experiment seems to be that the secondary rupture (dotted line) forming to the right of the primary rupture in the normal faulting experiment is not predicted in the analysis. However, since this rupture is not causing any noticeable deformation on the surface, one could argue that this difference is not that significant.

The comparison between analysis and experiment in terms of vertical displacement of the surface in Fig. 9 confirms the above argument (the horizontal distance, $d$, is measured from the point of application of the base offset; Fig. 7). Evidently, the numerical prediction is quite successful—not only the *location* of fault outcropping on the surface, but also the *localization* of the deformation within a narrow band match the experimental data points. For $h=0.2$ m (experiment: $h\approx0.25$ m), the analysis suggests a more or less quasielastic deformation of the ground surface, as suggested by Lade et al. (1984) and in accord with the experimental results. For $h=0.5$ m (experiment: $h\approx0.50$ m), the deformation starts becoming localized at a narrow band. Experimental results exhibit the same trend. Therefore, the analysis is successful in predicting the required minimum base dislocation for the fault to outcrop. The comparison remains totally satisfactory for higher levels of base dislocation. Observe that the images in the experiment were obtained for $h\approx0.25$, 0.50, 0.85, and 1.08 m rather than exactly 0.2, 0.5, 0.8, and 1.0 m, for which analysis results
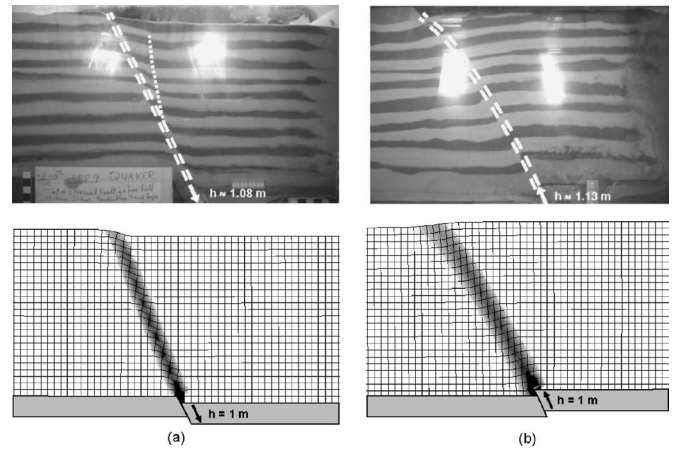


**Fig. 8.** Class A prediction—comparison of FE deformed mesh (with plastic strain concentration) against photographs from centrifuge experiments on medium-dense $D_r=80\%$ Fontainebleau sand: (a) normal faulting at 60° (Test 4); (b) reverse faulting at 60° (Test 3)

had already been publicized. We chose not to repeat the analyses for the laboratory imposed dislocation, so that the claim of prediction remained valid.

An image from Test 3 (reverse faulting) is compared to the deformed mesh of the analytical prediction in Fig. 8(b). The comparison is again quite satisfactory. Now, there is no secondary rupture and the numerically predicted deformation is almost indistinguishable from the experiment. Fig. 10 compares the analytical prediction with experimental results in terms of vertical displacement at the surface, for $h=0.2$, 0.5, 0.7, and 1.0 m (experiment: $h\approx0.18$, 0.49, 0.70, and 1.13 m, respectively). As for Test 4, we chose not to repeat the analyses for the laboratory imposed dislocation, so that the claim of a prediction remained valid. Admittedly, there is now a slight difference in the *location* of fault outcropping; the predicted location is about 3 m to the left
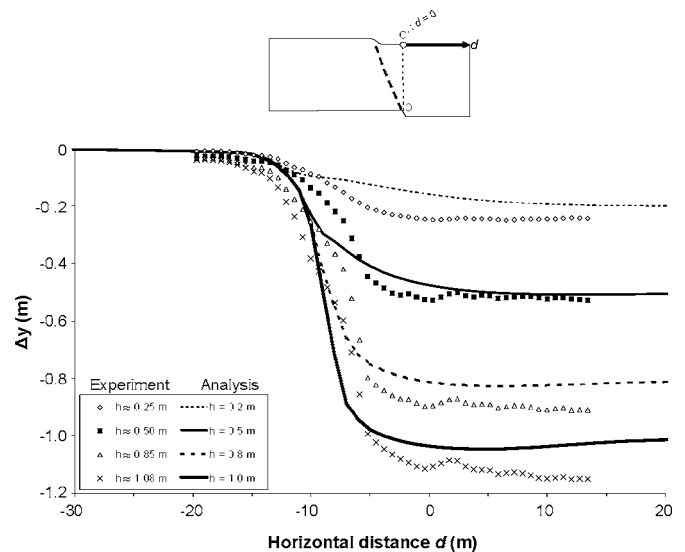


**Fig. 9.** Class A prediction of Test 4. Normal faulting at 60°, soil with $D_r=80\%$: comparison of numerical with experimental vertical displacement of the surface. Imposed bedrock dislocation $h=0.6$ and 1.0 m. Data from the experiment were obtained at $h\approx0.66$ and 1.1 m, respectively.
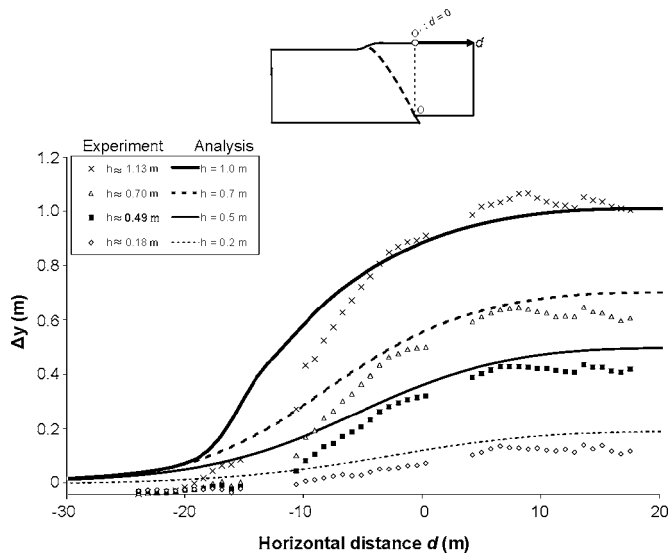
**Fig. 10.** Class A prediction of Test 3. Thrust faulting at 60°, soil with $D_r = 80\%$: comparison of numerical with experimental vertical displacement of the surface. Imposed bedrock dislocation $h = 0.2$ to $1.0$ m.

of the experiment. Overall, however, the prediction of the surface settlement profile remains satisfactory. As in Test 4, the numerical prediction is (reasonably) successful for all levels of imposed displacement. Note that the surface displacement profile measured by particle image velocimetry (PIV) analysis of the digital images taken in the centrifuge test was not of perfect quality because of lighting problems in this (early) test.

### Tests 12 and 8: Medium-Loose Fontainebleau Sand

Tests 12 (normal) and 8 (reverse) were conducted at 115$g$. Since the sand was medium-loose ($D_r = 60\%$), different model parameters were used to conduct the analytical predictions: $\varphi_p = 34°$, $\varphi_{res} = 30°$, $\psi_p = 6°$, $\gamma_y = 0.03$, $\gamma_p^P = 0.06$, and $\gamma_f^P = 0.244$ [applying Eq. (14), but with $n = 115$]. Model parameters were calibrated following the previously discussed calibration procedure, making use of direct-shear test data on Fontainebleau sand with $D_r = 60\%$ (El Nahas et al. 2006).

For Test 12 (normal faulting) the comparison in terms of vertical displacement at the surface is portrayed in Fig. 11(a), for $h$ ranging from 0.2 to 2.5 m. It is evident that the analysis foresees the correct location of fault outcropping, about 10 m from the vertical projection of the point of application of bedrock displacement, denoted as "$O'$," with discrepancies limited to 1 or 2 m at most. The deformation seems to be slightly more localized in the experiment, but the comparison between analytical and experimental thickness of the shear zone remains satisfactory.

For the smallest imposed dislocation, $h = 0.2$ m (experiment: $h \approx 0.24$ m), the analysis suggests a more or less quasielastic deformation at the surface, in accord with experimental results. For $h = 0.8$ m (experiment: $h \approx 0.797$ m), the deformation starts becoming localized in a relatively narrow band. Experimental results do not show as distinct a localization. In the FE analysis, the fault outcrops at $h \approx 1.0$ m, while in the experiment somewhere between $h = 0.99$ and 1.28 m. Therefore, the analysis is also successful in predicting the required minimum base dislocation for the fault to outcrop. The comparison remains satisfactory for higher levels of base dislocation. For $h = 2.5$ m (experiment: $h$
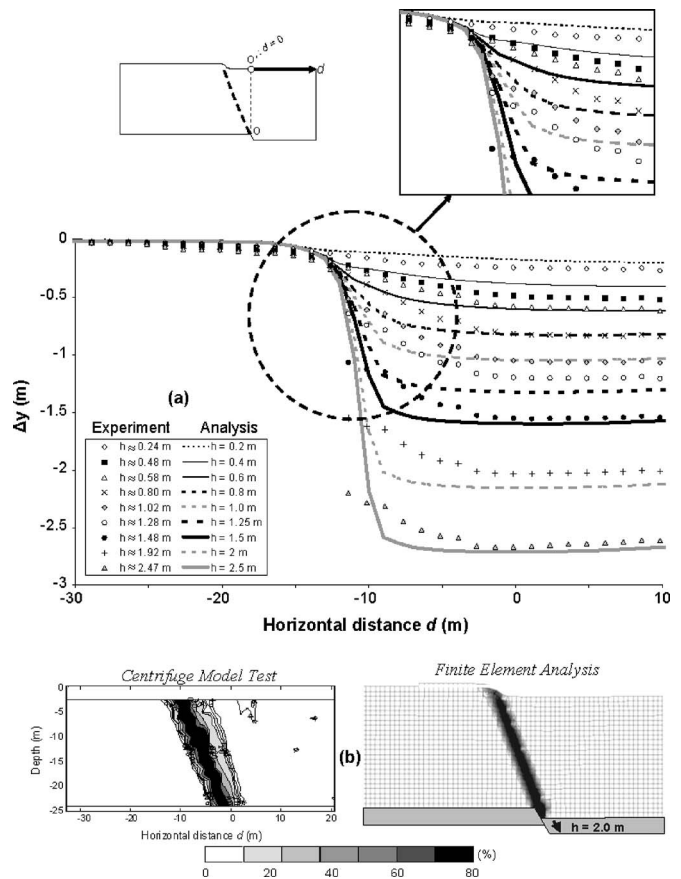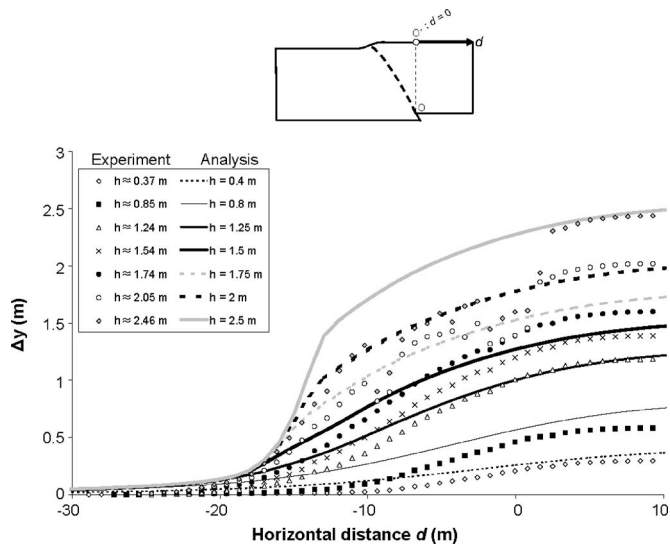


**Fig. 11.** Class A prediction of Test 12. Normal faulting at 60°, soil with $D_r = 60\%$: (a) comparison of numerical with experimental vertical displacement of the surface. Imposed bedrock dislocation $h = 0.2–2.5$ m; (b) comparison of experimental shear strain contours with FE deformed mesh with shear strain contours.

$\approx 2.47$ m) the localization in the experiment is just a little more intense and located about 0.5 m to the left (i.e., toward the footwall) compared to the analytical prediction. Overall, the analysis is quite satisfactory.

Centrifuge model test shear strain contours are compared with FE deformed mesh and shear strain contours in Fig. 11(b), for $h = 2.0$ m (experiment: $h \approx 1.92$ m). With the exception that experimental shear strain contours are a little more diffuse than the FE prediction, overall, the comparison can be claimed to be satisfactory.

The comparison of vertical displacement at the surface for Test 8 (reverse faulting) is depicted in Fig. 12, for the base dislocation $h$ ranging again from 0.2 to 2.5 m. As in the previous cases, the analysis is successful in predicting the location of fault outcropping. For $h = 0.4$ m (experiment: $h \approx 0.37$ m), experimental and analytical results exhibit a widespread quasielastic deformation of the surface: the fault has not yet outcropped. For $h = 1.75$ m, the deformation starts becoming localized in the analysis. The experimental results start showing signs of localization a little later, for $h \approx 2.05$ m. The analysis is again successful in predicting the displacement required at the base for the fault to outcrop: $h \approx 1.75$ m compared with the 2.05 m of the experiment. The comparison remains satisfactory for higher levels of imposed deformation. For $h = 2.5$ m (experiment: $h \approx 2.46$ m) the localization in the experiment is less intense, but always following a similar path

**Fig. 12.** Class A prediction of Test 8. Thrust faulting at 60°, soil with $D_r=80\%$: comparison of numerical with experimental vertical displacement of the surface. Imposed bedrock dislocation $h$ =0.4–2.5 m.

as the analysis. It is noted that for $h \geq 2$ m, poor centrifuge lighting conditions resulted in inaccurate experimental measurements.

### Sensitivity Analysis with Respect to Mesh Dependency and Scale Effects

Finite-element modeling in combination with strain-softening constitutive models may lead to mesh dependency, something that had already been investigated briefly before conducting the numerical predictions of centrifuge tests. Further corroboration of the developed FE methodology through a sensitivity study with respect to mesh density was deemed necessary. Experimental data are utilized as a yardstick to compare "objectively" the results of different FE meshes. Centrifuge experiments are reanalyzed using FE models with varying mesh density. In addition to the meshes of the initial sensitivity analysis (with $d_{FE}$ ranging from 0.5 to 5 m), an additional extremely finely meshed model, with $d_{FE}$ =0.25 m, is utilized.

Complete discussion of all results is beyond the scope of this paper. Hence, we focus on the results of Test 12 (normal faulting, medium-loose sand). Scale similarity is maintained through proper calibration of $\gamma_f^P$, using Eq. (14). More specifically, $\gamma_f^P$ =0.152, 0.244, and 0.796 for $d_{FE}$=2, 1, and 0.25 m, respectively. Fig. 13 compares two images from the experiment [Fig. 13(a)], for $h$=0.67 and 2.33 m, with corresponding FE deformed mesh with plastic strain for three different mesh sizes: 2 m [Fig. 13(b)], 1 m [Fig. 13(b)], and 0.25 m [Fig. 13(c)]. Evidently, the thickness of the shear zone *does* depend on *mesh size*, but the orientation of the propagation path is much less sensitive to mesh density: reducing $d_{FE}$ leads to slight progressive shift of the outcropping location towards the hanging wall, which is clear only in the comparison between the coarse mesh ($d_{FE}$=2 m) and the one selected for predictions ($d_{FE}$=1 m). The difference is hardly noticeable between 1 and 0.25 m meshes.

Fig. 14 compares experimental and numerical vertical displacement profiles for $h$=0.5, 1.0, and 1.5 m. As already deduced from Fig. 13, the thickness of the shear zone is reduced with reducing $d_{FE}$. In the coarse-meshed model ($d_{FE}$=2.0 m), the de-

formation is clearly less localized compared to the experiment. The 1 m meshed model compares well with the experiment in terms of both the outcropping location and the thickness of the shear zone. The finely meshed model ($d_{FE}$=0.25 m) yields even greater deformation localization, and even better fit with experimental data, but without a significant difference regarding the outcropping location.

Although centrifuge modeling is capable of reproducing prototype stress levels, it is not immune to scale effects (Palmer et al. 2003): the grain size cannot be scaled down. The latter has been shown to be a controlling parameter on the development and propagation of a rupture within a body of sand (Stone and Muir Wood 1992; Muir Wood 2002). To further investigate the degree of realism of the modeling methodology presented herein, trapdoor centrifuge model tests by White et al. (1994) are briefly analyzed and discussed. They refer to three model tests: two that maintain geometric similarity, and one that does not. Geometric similarity is maintained through scaling of physical parameters (depth $H$ and trapdoor displacement $h$) to $d_{50}$. Results are presented for the two geometrically similar tests: (1) $H$=75 mm and $d_{50}$=0.25 mm sand deposit, subjected to $h_{max}$=10 mm, at $150g$ centrifugal acceleration; and (2) $H$=150 mm and $d_{50}$=0.50 mm sand deposit, subjected to $h_{max}$=20 mm, at $75g$ centrifugal acceleration (all dimensions in model scale).

Based on the data reported by White et al. (1994), model parameters are roughly estimated as $\varphi_p$=49°, $\varphi_{res}$=35°, $\psi_p$=30°, $\gamma_y$=1.0%, and $\gamma_f$=0.17 and 0.28 for $d_{50}$=0.25 and 0.50 mm, respectively. The comparison of FE results with experimental data is depicted in Fig. 15. Initially, for $h/d_{50} \approx 12$, an initial rupture, R1, is formed at an angle of 25–30° to the vertical. Although R1 in the analysis is slightly steeper than in the experiment, both analysis and centrifuge testing agree that the rupture does not reach the surface. Increasing the imposed trapdoor downward displacement to $h/d_{50} \approx 22$, R1 becomes kinematically inadmissible and a secondary rupture, R2, is forced to develop. The latter propagates all the way to the surface. Finally, with further increase of $h/d_{50}$ to about 32, R2 becomes kinematically inadmissible and an almost vertical rupture, R3, propagates all the way to the surface. In all cases, the formation of each shear band coincides with ceasing of movement on the previous one. The analysis predicts well the location of rupture outcropping, and the required $h/d_{50}$ for each rupture either to propagate to the surface or become kinematically inadmissible, and the emergence and propagation of the ruptures. In general, the comparison between analysis and experiment is reasonably accurate.

### Parametric Study of Fault Rupture Propagation

Having validated the developed FE modeling methodology, we proceed to a parametric study of rupture propagation through sand, for normal and reverse faulting at dip angles $\alpha$=45 and 60°. The normalized [after Cole and Lade (1984)] vertical component of the imposed bedrock displacement, $h/H$, ranges from 0.25 to 5%, and from 0.5 to 10%, for normal and reverse faulting, respectively. For $H$=40 m, the above range of $h/H$ implies vertical offset values $h$=0.1–2 and 0.2–4 m, respectively. Based on the aforementioned calibration of Fontainebleau sand ($\varphi_{res}$, $\delta x_y$, $\delta x_p$, $\delta x_f$), a logical projection is conducted with respect to $\varphi_p$ and $\psi_p$, and two idealized soil materials are selected for parametric analysis:

- Loose sand: $\varphi_p$=32°, $\varphi_{res}$=30°, $\psi_p$=3°, $\gamma_y$=0.030, $\gamma_p^P$=0.06, and $\gamma_f^P$=0.0616; and
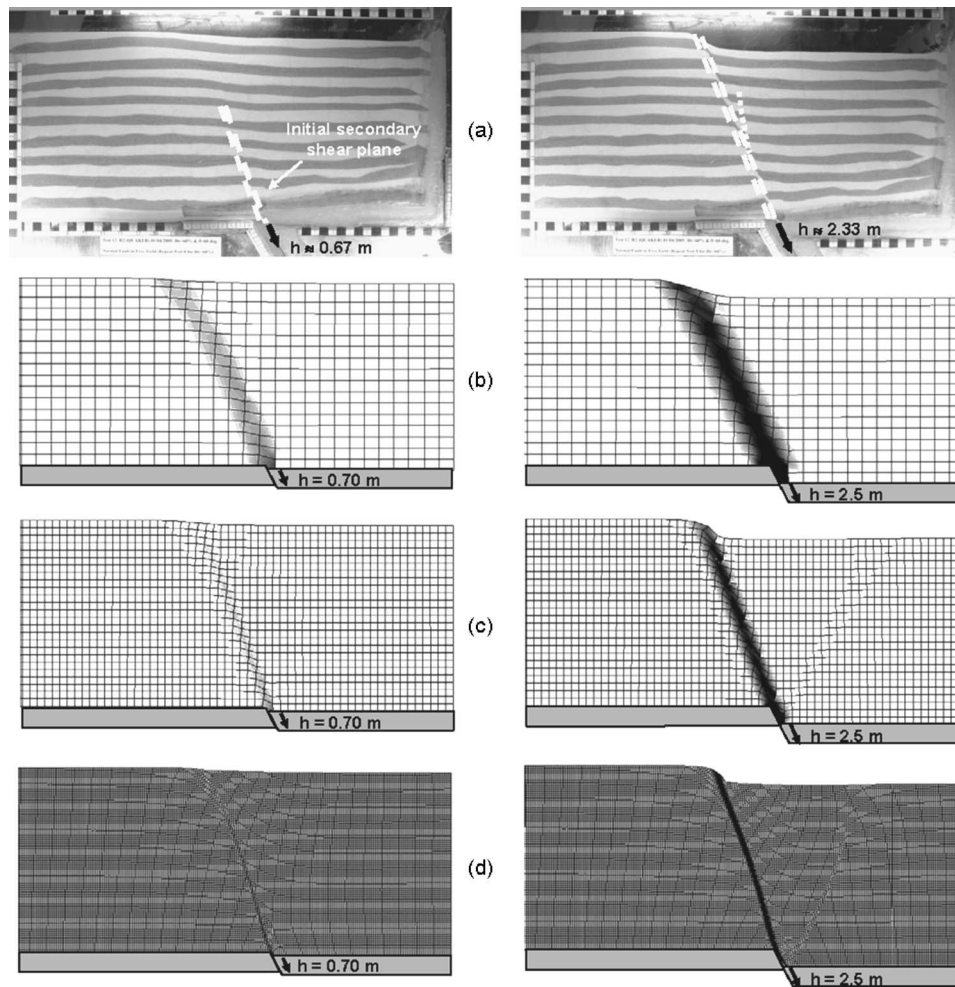
**Fig. 13.** Sensitivity analysis with respect to FE mesh density (Test 12: normal faulting at $60°$, $D_r = 60\%$): Comparison of experiment photographs (a) with deformed mesh and plastic strain concentration size; (b) 2 m; (c)1 m; and (d) 0.25 m

• Dense sand: $\varphi_p = 45°$, $\varphi_{res} = 30°$, $\psi_p = 18°$, $\gamma_y = 0.015$, $\gamma_p^P = 0.05$, and $\gamma_f^P = 0.0516$.

In both cases, $\gamma_f^P$ is computed through Eq. (14) with $n=1$ (prototype scale) and $d_{FE} = 1$ m.

### Normalization Issues

Snapshots of a propagating $\alpha = 45°$ normal fault rupture in a $H = 40$ m dense sand deposit are depicted in Fig. 16 in the form of deformed mesh with superimposed plastic strain (note that the hanging wall is now to the left). Darker regions denote higher plastic strains. Evidently, the dip increases significantly immediately after the rupture enters into the soil mass ("refraction" of the rupture path). Observe that only when the imposed normalized bedrock displacement $h/H$ exceeds 1% does the dislocation emerge on the ground surface. Increasing $h/H$ beyond 1.75% leads to development of a secondary *antithetic* rupture. Between primary and secondary rupture a gravity *graben* is formed. Further increase of $h/H$ (up to and beyond 5%) leads to deformation accumulation along the two ruptures, without additional changes.

It is emphasized that this antithetic secondary rupture constitutes an *extensional feature*, the mechanics of which are different from ordinary secondary ruptures. As already shown in the analysis of trapdoor experiments of White et al. (1994), movement on subsequent ruptures is associated with termination of activity on

previous dislocations. This feature, difficult to capture numerically, has already been shown to be accurately predicted through the developed FE methodology. The extensional antithetic rupture, discussed herein, does not coincide with termination of activity along the primary one. This behavior is consistent with experimental observations (Horsfield 1977; Cole and Lade 1984; Lade et al. 1984; Bray 1990).

Before proceeding with parametric analysis results, it must be shown that although analyses are conducted for $H = 40$ m, results and conclusions are of more general validity. As suggested by Cole and Lade (1984) and Bray (1990), and in accord with the principles of dimensional analysis (e.g., Muir Wood 2004), the deformation field (vertical and horizontal displacements) can be normalized with soil thickness $H$. To verify the validity of such normalization, the aforementioned analysis is repeated, but for $H = 20$ m. To maintain similarity with respect to mesh density, $d_{FE}$ is made equal to 0.5 m. Scale effects are taken into account through $\gamma_f^P$: since $d_{FE} = 0.5$ m, Eq. (14) yields $\gamma_f^P = 0.0532$. Results are compared in the form of normalized surface settlement $\Delta y/H$ in Fig. 17(a). Although the normalization is not strictly accurate (slight differences are observable), it can be seen as a reasonable approximation from an engineering point of view. Naturally, this result is due to the inherent assumptions of the developed simplified scaling method: preshear-band plastic strain is not scaled with $d_{FE}$.

To shed more light to scale effects, the same analysis (for $H = 40$ m) is repeated, but for a hypothetical centrifuge model test at $100g$ centrifugal acceleration. The model remains unaltered, with the only difference being $\gamma_f^P$: with $n=100$, Eq. (14) yields $\gamma_f^P = 0.21$. Now, scale effects can be clearly seen to play a major role. While in the prototype [Fig. 17(b)] the main rupture outcrops at $d/H=0.31$, in the hypothetical centrifuge model test [Fig. 17(c)] the fault break out takes place at $d/H=0.40$, i.e., the dislocation is less steep. The width of the fault graben is larger in the centrifuge test than in prototype (0.90 instead of 0.65), while the height of the fault scarp is inferior: $s/H=4.8\%$ instead of 5.9%. The required bedrock displacement for fault outcropping is also larger in the centrifuge (1.5% instead of 1%). These differences are attributable to unavoidable differences in mobilized dilation, which is significantly larger in the centrifuge test (where the grain size is unintentionally scaled-up $n$ times).

In conclusion, normalization with soil thickness $H$ can be a reasonable approximation. However, given that calibration of model parameters is based on Fontainebleau sand, analysis results can be claimed to be valid for fine-to-medium-grained sands with $d_{50}$ in the range of 0.5 mm. Care should be taken when projecting model test results to prototype scale: scale effects are shown to play a significant role.

### Surface Deformation and Location of Fault Outcropping

Normalized vertical displacement $\Delta y/H$ with respect to normalized distance $d/H$ (measured from $O'$) is depicted in Fig. 18 for normal faulting. For $\alpha=45°$, in dense sand [Fig. 18(a)] the main rupture emerges at normalized distance $d/H=0.31$ (i.e., for $H = 40$ m, $d \approx 12$ m). If the rupture had propagated at the same angle as the applied base rock dislocation, it would emerge at $d = H\tan 45° = 40$ m (i.e., $d/H=1$). It is evident that the rupture becomes significantly steeper while propagating through the soil mass. At this point, it is useful to define the "average" dip angle $\theta$ of the dislocation path in the soil

$$\theta = \tan^{-1}(H/d) \quad (15)$$

So, for dense sand subjected to $\alpha=45°$ normal faulting $\theta=73°$, which is significantly larger than $\alpha$. Naturally, the dislocation does not always propagate in a straight path: it often tends to further "refract" approaching the soil surface. Consequently, the average dip angle $\theta_{1/4}$ along the top 1/4 of $H$ is somewhat larger than $\theta$: $\theta_{1/4} \approx 75°$. However, $\theta$ is a useful indicator of the average deviation of the rupture path from the straight-line projection. In loose sand [Fig. 18(b)] the rupture emerges at larger distance from $O'$, at $d/H=0.68$, and $\theta \approx \theta_{1/4} \approx 56°$. Accordingly, for $\alpha = 60°$, the rupture emerges at $d/H \approx 0.30$ [Fig. 18(c)] and 0.63 [Fig. 18(d)] in dense and loose sand, respectively. The average dip angle $\theta$ is again equal to 73 and 58° in dense and loose sand, respectively. $\theta_{1/4}$ is only marginally larger in dense sand (74°).

A secondary antithetic rupture and a gravity graben are formed only for $\alpha=45°$ [Figs. 18(a and b)], in accord with the experimental observations of Horsfield (1977) and Cole and Lade (1984). The graben is wider in loose sand ($\approx 1.25H$) compared to dense sand ($\approx 0.65H$). The maximum $\Delta y/H$ is observed in dense sand at $\alpha=45°$ ($\approx 7\%$).

Fig. 19 illustrates $\Delta y/H$ with respect to $d/H$ for reverse faulting. For $a=45°$ the rupture outcrops at $d/H \approx 1.00$ [Fig. 19(a)] and 0.78 [Fig. 19(b)] in dense and loose sand, respectively. Note that the rupture tends to follow—on average—a straight-projection path (dense sand) or even increase its average dip when the dila-
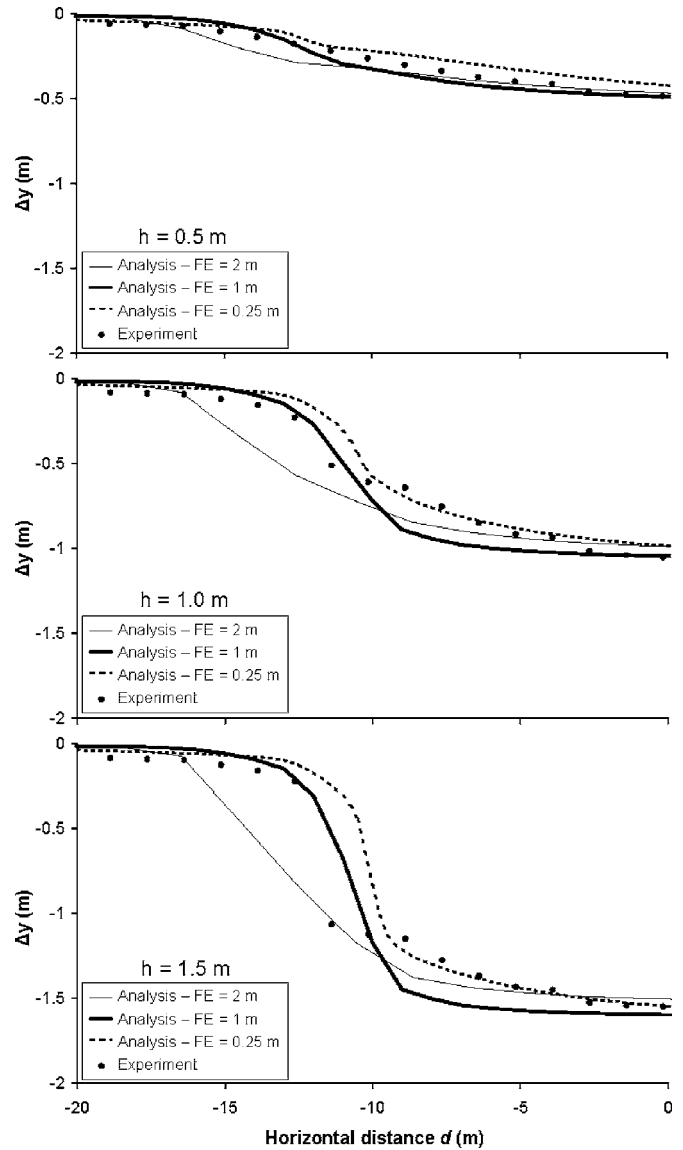


**Fig. 14.** Sensitivity analysis with respect to FE mesh density (Test 12: normal faulting at 60°, $D_r=60\%$): comparison of vertical displacement profiles

tion angle $\psi_p$ is low ($\theta=52° > \alpha=45°$, in loose sand), in accord with the small-scale experiments of Lade et al. (1984). $\theta_{1/4}$ is practically the same in dense sand (44°) and slightly less in loose sand (49°). Although field evidence suggests that reverse faults usually decrease in dip propagating to the surface, such behavior can be explained following the hypothesis of Prucha et al. (1965). According to their theory, when horizontal compression is prevailing ($\alpha \leq 45°$), the fault dip tends to increase as the rupture propagates to the surface, becoming concave when viewed from the hanging wall. In contrast, if vertical differential uplifting is the prevailing mechanism ($\alpha > 45°$), then the dip will tend to decrease, becoming convex. The 45° dip allows for significant horizontal compression, but also vertical uplift. It can be seen as an intermediate limiting case, in which both factors are equally important. If this reasoning is valid, and provided that the numerical modeling technique is realistic, the rupture should be expected to bend more toward the footwall for $\alpha=60°$.

Figs. 19(c and d) depict the results for $\alpha=60°$. The rupture outcrops at $d/H \approx 0.80$ [Fig. 19(c)] and 0.65 [Fig. 19(d)] in dense
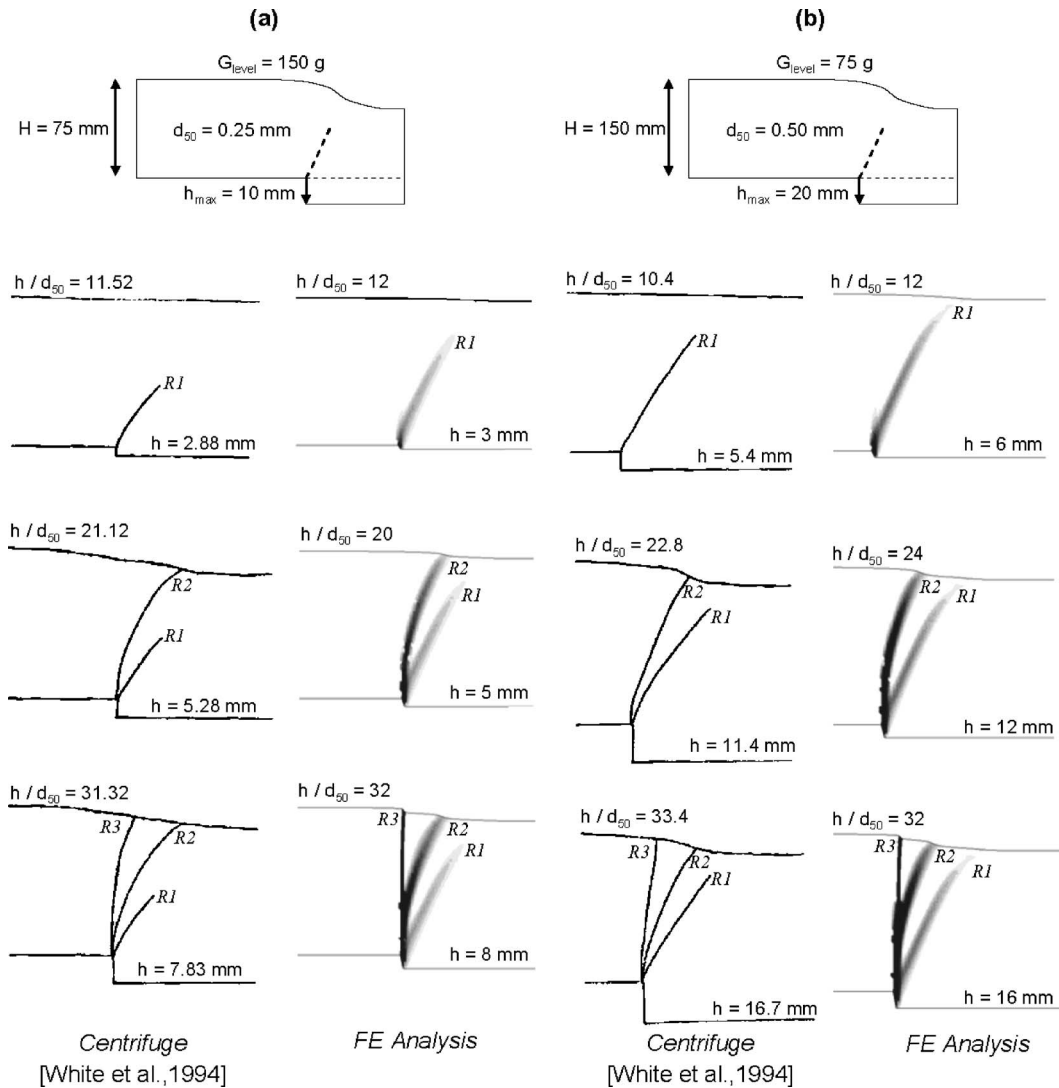
**Fig. 15.** Validation of simplified scaling methodology: comparison of analysis with centrifuge trapdoor model test of White et al. (1994): (a) $H=75$ mm, $d_{50}=25$ mm sand deposit, subjected to $h_{max}=10$ mm downward displacement at $150g$ centrifugal acceleration; (b) $H_{50}=150$ mm, $d_{50}=50$ mm sand deposit, subjected to $h_{max}=20$ mm downward displacement at $75g$ centrifugal acceleration (all dimensions in model scale). Similarity is maintained through scaling of $H$ and $h$ to $d_{50}$.

and loose sand, respectively. Now that vertical differential uplifting is the prevailing mechanism, the rupture can be seen to bend more over the footwall, decreasing its dip in all cases: $\theta=51$ and $57°$ in dense and loose sand, respectively (i.e., $\theta < \alpha=60°$). $\theta_{1/4}$ is slightly less ($49°$) in dense sand, but significantly lower in loose sand ($53°$).

### Required Bedrock Displacement for Fault Outcropping

The required bedrock displacement for the fault to outcrop is a crucial parameter for the design of structures overlying active faults. If $h/H$ is not enough for the fault to outcrop, an overlying structure will only be subjected to a smooth distributed differential settlement (which, however, may still be damaging). In stark contrast, when $h/H$ is large enough for the rupture to outcrop, a fault scarp is created and differential displacement is localized in a narrow zone. Obviously, the damage potential will be substantially larger in such a case.

In normal faulting [Figs. 18 and 20(a and b)], the required bedrock displacement for fault outcropping ranges from
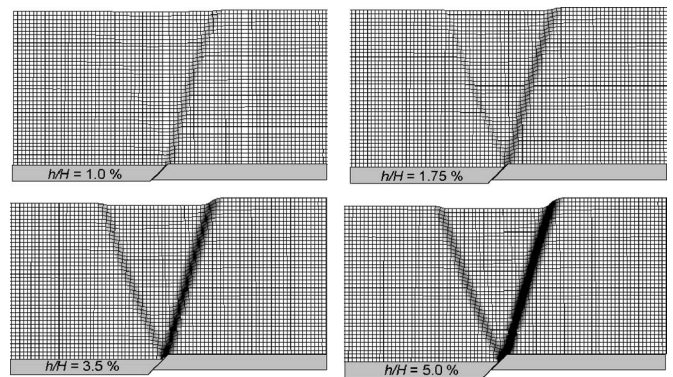


**Fig. 16.** Snapshots of deformed mesh and plastic strain due to normal faulting at $\alpha=45°$ for base dislocation $h=0.4$, 0.7, 1.4, and 2 m in dense sand ($\varphi=45°$, $\psi=18°$, and $\gamma_y=1.5\%$)
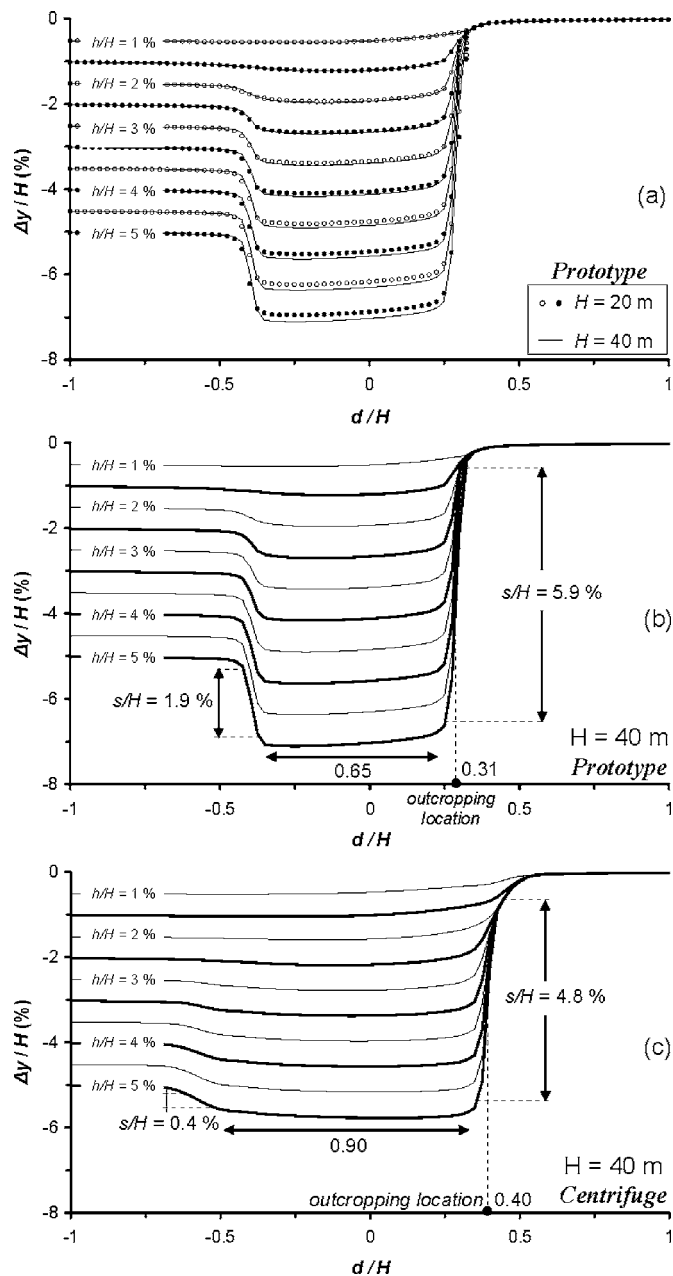
**Fig. 17.** Normalized vertical displacement $\Delta y/H$ at the soil surface with respect to normalized horizontal displacement $d/H$ for normal fault rupture with $\alpha=45°$ in idealized dense sand ($\varphi=45°$, $\psi=18°$, and $\gamma_y=1.5\%$): (a) Simulation of prototype, comparison of results for $H=40$ and 20 m. The normalization, although not completely accurate, is reasonable from an engineering point of view; (b) Simulation of $H=40$ m prototype; compared to (c) hypothetical centrifuge model test at 100$g$. Scale effects play a significant role.

$h/H \approx 0.75\%$ in dense sand to 1.00% in loose sand. Loose sand tends to "elastically" deform more, "delaying" the emergence of the fault rupture on the surface, as suggested by experimental observations of Cole and Lade (1984), Lade et al. (1984), and Bray (1990). Secondary ruptures (for $\alpha=45°$) reach the surface at larger imposed normalized vertical displacement: $h/H\approx1.5$ and 2.5% in dense and loose sand, respectively. The results are qualitatively similar in reverse faulting [Figs. 19 and 20(c and d)]. Naturally, due to the difference in kinematics (passive instead of

active conditions), the required bedrock displacement for fault outcropping is about three times larger: $h/H \approx 2.5\%$ in dense sand and 4.0% in loose sand.

### Scarp Height

Figs. 20(a and b) plot the normalized fault scarp height $s/h$ (i.e., $s/H$ divided by $h/H$) versus $h/H$, for dense and loose sand subjected to normal faulting. In both cases, $s/h$ is initially equal to zero (before fault outbreak), increases abruptly after $h/H$ =0.75% (in dense sand) to 1.0% (in loose sand), and reaches an "asymptote" at higher dislocation levels. For $\alpha=60°$, the maximum $s/h$ reaches 84 and 56% for dense and loose sand, respectively. In loose sand, the soil deforms more quasielastically, converting a greater portion of the imposed dislocation to widely spread differential settlement, and thus reducing the scarp height. For $\alpha=45°$, $s/h$ is larger in both sands (117 and 82%) due to formation of the secondary antithetic rupture and the graben. The height of secondary fault scarps reaches $s/h=9$ and 37% in dense and loose sand, respectively. In dense sand, the difference in $s/h$ of the primary fault scarp between $\alpha=45$ and 60° is roughly equal to the height of the secondary fault scarp.

The situation is similar in reverse faulting [Figs. 17(c and d)]. As in normal faulting, for relatively small $h/H$ the rupture cannot reach the surface, while after outcropping most of the deformation accumulates along the localization. In both sands, $s/h$ is initially zero, increasing abruptly after $h/H=2.5$–4%, and tends to stabilize at higher $h/H$ levels. As expected, $s/h$ is significantly higher for dense than for loose sand. For instance, the asymptotic values are of the order of 80–90% for dense sand, compared with 50–60% in loose sand, for $\alpha=60$ and 45°, respectively. The increase of $s/h$ with decreasing $\alpha$ can be attributed to the enhanced role of horizontal compression. In other words, with $\alpha=45°$ increased horizontal compression develops, leading to amplified dilation; at high deformation levels this causes an increase of $s$, in contrast to normal faulting where increased dilation was shown to reduce it. In normal faulting the dilation leads to partial compensation of the differential settlement, reducing $s$. While the hanging wall is being displaced downwards, the dilation mobilizes action in the opposite direction (upwards). In reverse faulting, dilation amplifies the differential uplift: the hanging wall is being displaced upwards, and the dilation acts to further increase it.

### Limitations

The present study has certain limitations:

1. The mean grain size, $d_{50}$, has been shown to be a controlling parameter in the propagation of dislocations through sand (Muir Wood 2002). The mobilized dilation volume depends on the thickness of the shear band. In this study, scale effects are incorporated in the developed FE model only in an approximate manner. Based on published research (Jewell and Roth 1987; Gerolymos et al. 2007), the shear band is assumed to form only after peak conditions are reached. Thus, scaling is not applied to the pre-shear-band parameters $\gamma_y$ and $\gamma_p$ of the constitutive model—undoubtedly a simplification of a more complex reality.

2. For a given sand, normalization with soil thickness $H$ is a reasonable approximation. However, in this study calibration of model parameters is based on Fontainebleau sand. Hence, analysis results can be claimed to be valid for fine-to-medium-grained sands with $d_{50}$ in the range $\approx 0.5$ mm. Care
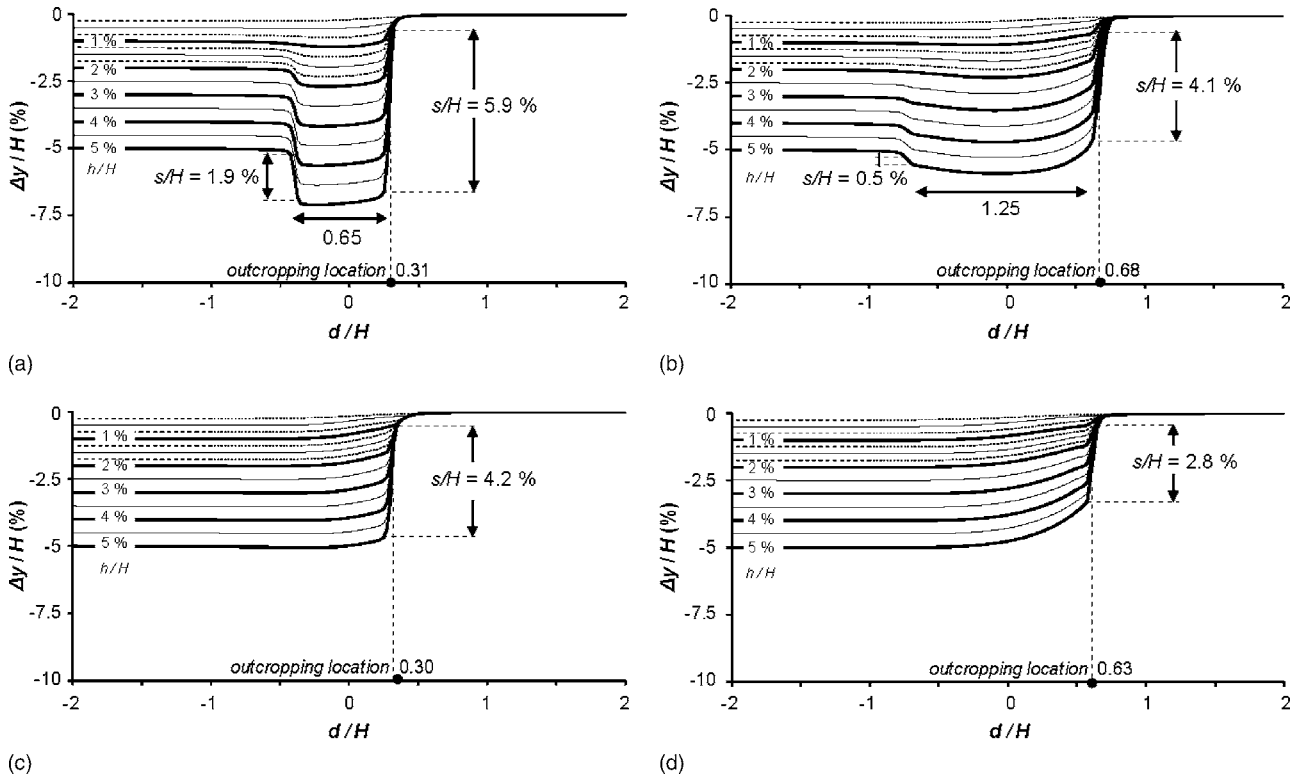
**Fig. 18.** Normal faulting: normalized vertical displacement $\Delta y/H$ at the ground surface for normalized bedrock displacement ranging from $h/H=0.25$ to 5% for (a) $\alpha=45°$, dense sand; (b) $\alpha=45°$, loose sand; (c) $\alpha=60°$, dense sand; and (d) $\alpha=60°$, loose sand (dense sand: $\gamma_y=1.5\%$, $\varphi=45°$, and $\psi=18°$; loose sand; $\gamma_y=3\%$, $\varphi=32°$, and $\psi=3°$)
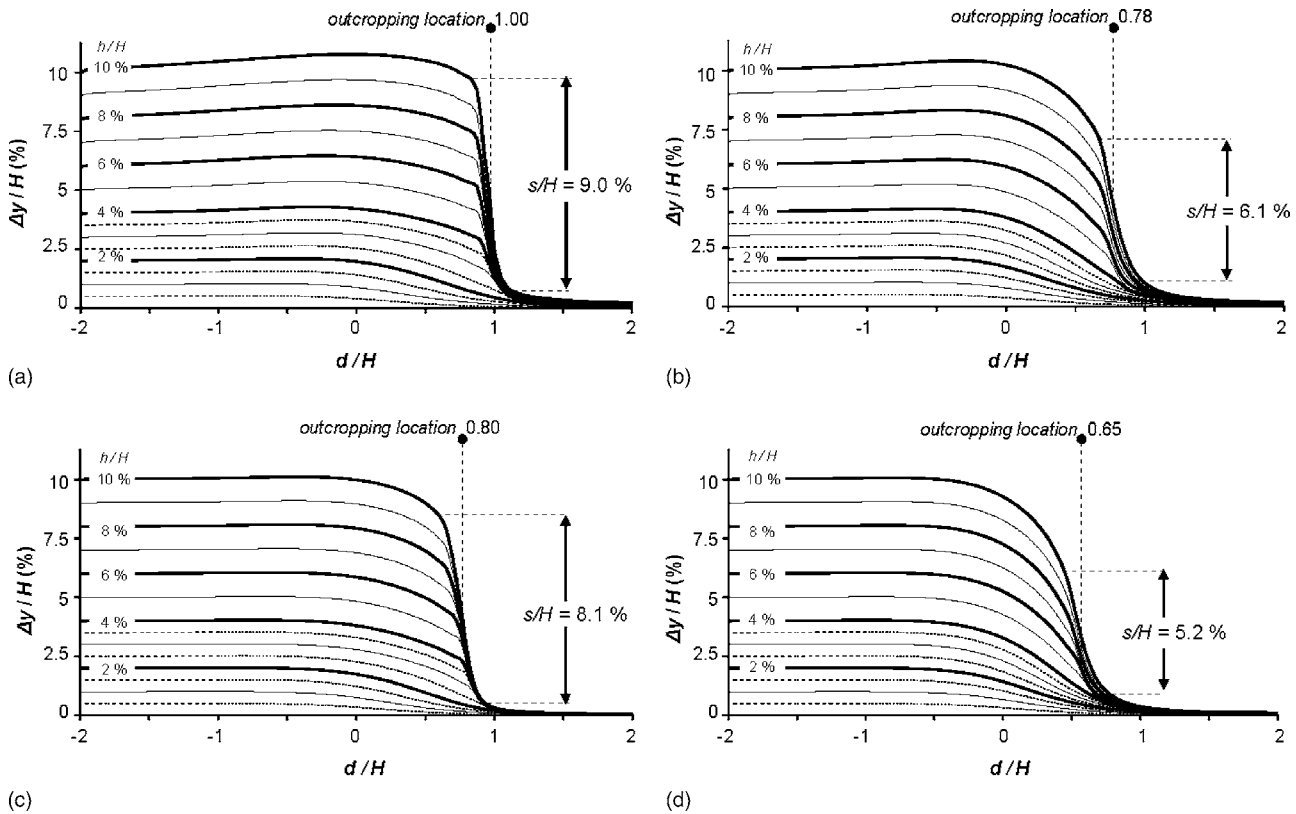


**Fig. 19.** Reverse faulting: normalized vertical displacement $\Delta y/H$ at the ground surface for normalized bedrock displacement ranging from $h/H=0.5$ to 10% for: (a) $\alpha=45°$, dense sand; (b) $\alpha=45°$, loose sand; (c) $\alpha=60°$, dense sand; and (d) $\alpha=60°$, loose sand (dense sand: $\varphi=45°$, $\psi=18°$, and $\gamma_y=0.5\%$; loose sand: $\varphi=32°$, $\psi=3°$, and $\gamma_y=3\%$)
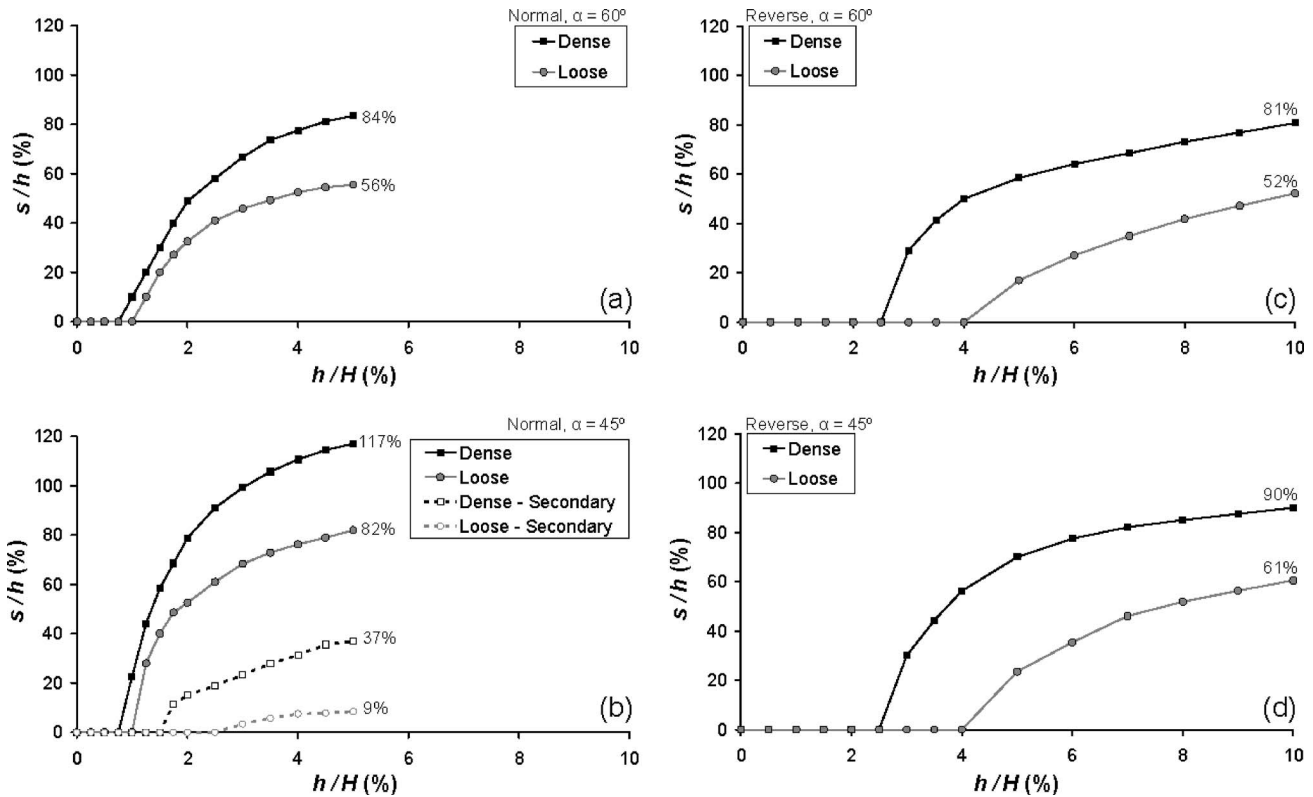
**Fig. 20.** Normalized fault scarp height $s/h$ versus normalized bedrock displacement $h/H$: (a) normal fault at $\alpha=60°$; (b) normal fault $\alpha=45°$; (c) reverse fault at $\alpha=60°$; and (d) reverse fault $\alpha=45°$ (dense sand: $\varphi=45°$, $\psi=18°$, and $\gamma_y=1.5\%$; loose sand: $\varphi=32°$, $\psi=3°$, and $\gamma_y=3\%$)

should be exercised when projecting model test results to prototype scale: scale effects are shown to play a significant role.

3. In all cases, both in the centrifuge and in the analysis, the sand is dry. In real conditions, a water table is likely to be present, and the response may be altered due to the existence of transient pore water pressures for fast deformations or different effective stress conditions. Such issues are not addressed in this paper and further research would be desirable.

## Conclusions

1. This paper provides validated analytical data for the design of structures on top of active faults. Emphasis is given to results that are useful in engineering, such as: (a) the location of fault outcropping; (b) the vertical displacement profile of the ground surface; and (c) the minimum fault offset at bedrock necessary for the rupture to reach the ground surface.

2. Validation of the numerical methodology is achieved through extensive comparisons of Class A predictions with results of four centrifuge experiments. The developed modeling technique predicted with sufficient accuracy both the location of fault outcropping and the displacement profile at the ground surface, giving confidence in the methodology and the results obtained in this paper.

3. Further validation is provided through analysis of trapdoor centrifuge model tests of White et al. (1994). The developed analysis methodology is shown to predict successfully all experimental observations. Movement on subsequent rup-

tures is shown to be associated with termination of activity on previous dislocations, a feature that is generally quite difficult to capture numerically.

4. Normal fault ruptures tend to bend over the hanging wall, increasing their dip angle. A large portion of this increase takes place at the soil–bedrock interface, a phenomenon reminiscent of the refraction of seismic waves. Then, propagating to the surface, the dip increases further. The increase of $\varphi_p$ and $\psi_p$ causes further bending of the fault rupture.

5. In general, reverse fault ruptures tend to bend over the footwall, decreasing their dip angle. Increasing $\varphi_p$ and $\psi_p$ decreases the average dip angle $\theta$. However, when $a \leq 45°$ the dip may remain constant or even increase, in accord with the theory of Prucha et al. (1965) and the small-scale experiments of Lade et al. (1984). When the prevailing mechanism is differential uplifting ($a > 45°$), the dip decreases and the rupture bends more over the footwall.

6. As first demonstrated by Bray (1990), the required bedrock offset ratio $h/H$ to propagate the rupture to the surface is an increasing function of soil ductility, expressed in the constitutive model through $\gamma_y$ and $\gamma_f$. In normal faulting, and for the dip angles investigated herein ($\alpha=45$ and $60°$), the required $h/H$ for fault outcropping ranges from 0.75% in dense to 1.0% in loose sand. In reverse faulting, due to the difference in kinematics (passive instead of active conditions), it is about three times larger: 2.5% in dense and 4.0% in loose sand.

7. When the fault dip $a$ is relatively small [$a < 45° + \psi/2$, after Cole and Lade (1984)], an antithetic secondary rupture and a gravity graben are formed. The antithetic rupture outcrops for larger $h/H$ than for the primary one: 1.5% in dense and

2.5% in loose sand. Its width is a decreasing function of $\varphi_p$ and $\psi_p$: $0.65H$ in dense and $1.25H$ in loose sand.

8. The height of the fault scarp $s$, for a specific bedrock imposed displacement $h/H=$decreasing function of both soil ductility and dilation angle $\psi_p$. The normalized fault scarp $s/h$ is a function of $h/H$. In normal faulting, for $a=60°$, no antithetic rupture is formed and $s/h$ reaches 56 and 84% for loose and dense sand, respectively. For $a=45°$, a graben is developed, and $s/h$ ranges from 82 to 117% in loose and dense sand, respectively. In reverse faulting for $\alpha=60°$, $s/h$ reaches 52 and 81%, for dense and loose sand, respectively. For $\alpha=45°$, $s/h$ is somewhat larger, reaching 61% in loose and 90% in dense sand.

## Acknowledgments

## References

ABAQUS, Inc. (2004). *ABAQUS V.6.4 user's manual*, Providence, R.I.

Anastasopoulos, I. (2005). "Fault rupture–soil–foundation–structure interaction." Ph.D. dissertation, School of Civil Engineering, National Technical Univ., Athens, Greece.

Ambraseys, N., and Jackson, J. (1984). "Seismic movements.." *Ground movements and their effects on structures*, P. B. Attewell and R. K. Taylor, eds., Surrey University Press, Surrey, U.K., 353–380.

Bažant, Z. P., and Tsang, T. P. (1984). "Nonlocal finite-element analysis of strain softening solids." *J. Eng. Mech.* 110(12), 1441–1450.

Bray, J. D. (1990). "The effects of tectonic movements on stresses and deformations in earth embankments." Ph.D. dissertation, Univ. of California at Berkeley, Berkeley, Calif.

Bray, J. D., Seed, R. B., and Seed, H. B. (1993). "1*g* small-scale modeling of saturated cohesive soils." *Geotech. Test. J.*, 16(1), 46–53.

Bray, J. D., Seed, R. B., Cluff, L. S., and Seed, H. B. (1994a). "Earthquake fault rupture propagation through soil." *J. Geotech. Engrg.*, 120(3), 543–561.

Bray, J. D., Seed, R. B., and Seed, H. B. (1994b). "Analysis of earthquake fault rupture propagation through cohesive soil." *J. Geotech. Engrg.*, 120(3), 562–580.

Budhu, M. (1984). "Nonuniformities imposed by simple shear apparatus." *Can. Geotech. J.*, 21(1), 125–137.

Cole, D. A., Jr., and Lade, P. V. (1984). "Influence zones in alluvium over dip–slip faults." *J. Geotech. Engrg.*, 110(5), 599–615.

de Borst, R. (1991). "Simulation of strain localization: A reappraisal of the Cosserat continuum." *Eng. Comput.*, (8), 317–332.

El Nahas, A., Bransby, M. F., and Davies, M. C. R. (2006). "Centrifuge modeling of the interaction between normal fault rupture and rigid, strong raft foundations." *Proc., Int. Conf., on Physical Modeling in Geotechnics*, Hong Kong, August, 337–342.

Erickson, S. G., Staryer, L. M., and Suppe, J. (2001). "Initiation and reactivation of faults during movement over a thrust-fault ramp: Numerical mechanical models." *J. Struct. Geol.*, 23, 11–23.

Gaudin, C. (2002). "Experimental and theoretical study of the behavior of supporting walls: Validation of design methods." Ph.D. dissertation, Laboratoire Central des Ponts et Chaussées, Nantes, France.

Gerolymos, N., Vardoulakis, I., and Gazetas, G. (2007). "A thermo-poro-visco-plastic shear band model for seismic triggering and evolution of

catastrophic landslides." *Soils Found.*, 47(1), 11–26.

Gudehus, G., and Nübel, K. (2004). "Evolution of shear bands in sand." *Geotechnique*, 54(3), 187–201.

Horsfield, W. T. (1977). "An experimental approach to basement-controlled faulting." *Geol. Mijnbouw*, 56(4), 363–370.

Jewell, R. A. (1989). "Direct shear tests on sand." *Geotechnique*, 39(2), 309–322.

Jewell, R. A., and Roth, C. P. (1987). "Direct shear tests on reinforced sand." *Geotechnique*, 37(1), 53–68.

Lade, P. V., Cole, D. A., Jr., and Cummings, D. (1984). "Multiple failure surfaces over dip–slip faults." *J. Geotech. Engrg.*, 110(5), 616–627.

Lambe, T. W. (1973). "Predictions in soil engineering." *Geotechnique*, 23(2), 149–202.

Loret, B., and Prevost, H. J. (1990). "Dynamic strain localization in elasto-(visco)-plastic solids. Part 1: General formulation and one-dimensional examples." *Comput. Methods Appl. Mech. Eng.*, 83(3), 247–273.

Loukidis, D. (1999). "Active fault propagation through soil." Thesis, School of Civil Engineering, National Technical Univ., Athens, Greece.

Morgenstern, N. R., and Tchalenko, J. S. (1967). "Microscopic structures in Kaolin subjected to direct shear." *Geotechnique*, 17(4), 309–328.

Mühlhaus, H.-B., and Vardoulakis, I. (1987). "The thickness of shear bands in granular materials." *Geotechnique*, 37(3), 271–283.

Muir Wood, D. (2002). "Some observations of volumetric instabilities in soils." *Int. J. Solids Struct.*, 39, 3429–3449.

Muir Wood, D. (2004). *Geotechnical modeling*, E&F Spon, London.

Muir Wood, D., and Stone, K. J. L. (1994). "Some observations of zones of localization in model tests on dry sand." *Localization and bifurcation theory for soils and rocks*, R. Chambon, J. Desrues, and I. Vardoulakis, eds., Balkema, Rotterdam, The Netherlands, 155–164.

Nakai, T., Muir Wood, D., and Stone, K. J. L. (1995). "Numerical calculations of soil response over a displacing basement." *Soils Found.*, 35(2), 25–35.

Palmer, A. C., et al. (2003). "Uplift resistance of buried submarine pipelines: Comparison between centrifuge modelling and full-scale tests." *Geotechnique*, 53(10), 877–883.

Pietruszezak, S. T., and Mroz, Z. (1981). "Finite-element analysis of deformation of strain softening materials." *Int. J. Numer. Methods Eng.*, 17, 327–334.

Potts, D. M., Dounias, G. T., and Vaughan, P. R. V. (1987). "Finite-element analysis of the direct shear box test." *Geotechnique*, 37(1), 11–23.

Potts, D. M., Dounias, G. T., and Vaughan, P. R. (1990). "Finite-element analysis of progressive failure of Carsington embankment." *Geotechnique*, 40(1), 79–101.

Potts, D. M., Kovacevic, N., and Vaughan, P. R. (1997). "Delayed collapse of cut slopes in stiff clay." *Geotechnique*, 47(5), 953–982.

Prucha, J. J., Graham, J. A., and Nickelsen, R. P. (1965). "Basement-controlled deformation in Wyoming province of Rocky Mountains foreland." *Am. Assoc. Pet. Geol. Bull.*, 49(7), 966–992.

Roth, W. H., Sweet, J., and Goodman, R. E. (1982). "Numerical and physical modeling of flexural slip phenomena and potential for fault movement." *Rock Mech.*, 12, 27–46.

Saada, A. S., and Townsend, F. C. (1981). "State of the art: Laboratory strength testing of soils." *ASTM Special Technical Publication 740*, ASTM, West Conshohocken, Pa., 7–77.

Scott, R. F., and Schoustra, J. J. (1974). "Nuclear power plant sitting on deep alluvium." *J. Geotech. Engrg. Div.*, 100(4), 449–459.

Shibuya, S., Mitachi, T., and Tamate, S. (1997). "Interpretation of direct shear box testing of sands as quasisimple shear." *Geotechnique*, 47(4), 769–790.

Stone, K. J. L., and Muir Wood, D. (1992). "Effects of dilatancy and particle size observed in model tests on sand." *Soils Found.*, 32(4), 43–57.

Terzaghi, K., and Peck, R. B. (1948). *Soil mechanics in engineering practice*, Wiley, New York.

Vardoulakis, I., and Graf, B. (1985). "Calibration of constitutive models

for granular materials using data from biaxial experiments." *Geotechnique*, 35(3), 299–317.

Walters, J. V., and Thomas, J. N. (1982). "Shear zone development in granular materials." *Proc., 4th Int. Conf. on Numerical Methods in Geomechanics*, Vol. I, Edmonton, Canada, 263–274.

White, D. J., Take, W. A., and Bolton, M. D. (2003). "Soil deformation measurement using particle image velocimetry (PIV) and photogrammetry." *Geotechnique*, 53(7), 619–631.

White, R. J., Stone, K. J. L., and Jewel, R. J. (1994). "Effect of particle size on localization development in model tests on sand." *Proc., Inst. Centrifuge Conf.*, C. F. Leung, F. H. Lee, and T. S. Tan, eds., Balkema, Rotterdam, The Netherlands, 817–822.